Machine Learning–Based Computational Models Derived From Large-Scale Radiographic-Radiomic Images Can Help Predict Adverse Histopathological Status of Gastric Cancer

Qiong Li, MMed[1], Liang Qi, MD[1], Qiu-Xia Feng, MMed[1], Chang Liu, MMed[1], Shu-Wen Sun, MMed[1], Jing Zhang, MD[2], Guang Yang, PhD[2], Ying-Qian Ge, MSc[3], Yu-Dong Zhang, MD, PhD[1] and Xi-Sheng Liu, MD[1]

INTRODUCTION: **Adverse histopathological status (AHS) decreases outcomes of gastric cancer (GC). With the lack of a single factor with great reliability to preoperatively predict AHS, we developed a computational approach by integrating large-scale imaging factors, especially radiomic features at contrast-enhanced computed tomography, to predict AHS and clinical outcomes of patients with GC.**

METHODS: **Five hundred fifty-four patients with GC (370 training and 184 test) undergoing gastrectomy were retrospectively included. Six radiomic scores (R-scores) related to pT stage, pN stage, Lauren & Borrmann (L&B) classification, World Health Organization grade, lymphatic vascular infiltration, and an overall histopathologic score (H-score) were, respectively, built from 7,000+ radiomic features. R-scores and radiographic factors were then integrated into prediction models to assess AHS. The developed AHS-based Cox model was compared with the American Joint Committee on Cancer (AJCC) eighth stage model for predicting survival outcomes.**

RESULTS: **Radiomics related to tumor gray-level intensity, size, and inhomogeneity were top-ranked features for AHS. R-scores constructed from those features reflected significant difference between AHS-absent and AHS-present groups ($P < 0.001$). Regression analysis identified 5 independent predictors for pT and pN stages, 2 predictors for Lauren & Borrmann classification, World Health Organization grade, and lymphatic vascular infiltration, and 3 predictors for H-score, respectively. Area under the curve of models using those predictors was training/test 0.93/0.94, 0.85/0.83, 0.63/0.59, 0.66/0.63, 0.71/0.69, and 0.84/0.77, respectively. The AHS-based Cox model produced higher area under the curve than the eighth AJCC staging model for predicting survival outcomes. Furthermore, adding AHS-based scores to the eighth AJCC staging model enabled better net benefits for disease outcome stratification.**

DISCUSSION: **The developed computational approach demonstrates good performance for successfully decoding AHS of GC and preoperatively predicting disease clinical outcomes.**

SUPPLEMENTARY MATERIAL accompanies this paper at http://links.lww.com/CTG/A94

Clinical and Translational Gastroenterology 2019;10:e00079. https://doi.org/10.14309/ctg.0000000000000079

INTRODUCTION

Gastric cancer (GC) is the fifth most common cancer and the second leading cause of cancer death worldwide (1). Although the incidence of GCs worldwide has generally declined in recent decades, the 5-year survival rate is still not optimistic (2). Generally, the 5-year survival rate of GCs was found to be significantly correlated with TNM (tumor, lymph node, and metastatic) staging (3–5). However, there were also large variations in clinical outcomes among patients receiving similar treatment at the same TNM stage (4,6). An increasing number of studies have found different histopathological types are closely related to the prognosis of GCs. Studies have found patients with medium and

[1]Department of Radiology, the First Affiliated Hospital with Nanjing Medical University, Nanjing, China; [2]Shanghai Key Laboratory of Magnetic Resonance, East China Normal University, Shanghai, China; [3]CT Scientific Marketing, Siemens Healthcare, Shanghai, China. **Correspondence:** Yu-Dong Zhang, MD, PhD. E-mail: njmu_zyd@163.com. Xi-Sheng Liu, MD. E-mail: njmu_lxs@163.com.

Received March 19, 2019; accepted August 5, 2019; published online October 2, 2019

poorly differentiated carcinomas, signet ring cell carcinomas, and mucinous carcinomas (histopathological type according to the World Health Organization [WHO] classification) are proved to be more aggressive (7–11). Previous studies indicated that diffuse type (histopathological type according to Lauren classification) and Borrmann type IV (histopathological type according to Borrmann classification) patients were associated with poor prognosis (7,12–14). Besides, several studies demonstrated that lymphatic vascular infiltration (LVI) of the tumor is an additional prognostic marker (6,7,15,16). Taken together, the histopathological status is an important risk factor and exerts excellent ability to classify survival of patients with GCs. If high-risk patients are identified before radical gastrectomy, individualized treatment regimens can be provided for these patients. Hence, it is very important to establish preoperative biomarkers and/or signatures for decoding histopathological status and predicting the postoperative outcomes of patients with locally advanced GCs.

Currently, preoperative endoscopic biopsy is usually used to obtain histopathological results of GC. However, endoscopic biopsy is invasive and subjective to evaluate the tumor stage and histopathological status, and there are no uniform guidelines for biopsy specimen identification (17). The role of computed tomography (CT), even if controversial, can show the site, shape, and depth of infiltration of a tumor, which is fundamental for evaluating T and N stages of the gastric disease (3,18,19). Recently, several studies have shown the preoperative implications of CT findings for GCs' histopathological status (16,20,21). But despite encouraging results in recent clinical studies have been demonstrated, expert-level performance of radiographic imaging for gastric disease is still controversial, and a variety of imaging findings have been described with variable examination utilities. Previously described morphologic or functional methods at CT or magnetic resonance images have shown inconsistent reproducibility. Therefore, task difficulties remain about how to best design adequate measurement that achieves the goals of risk communication to enable lesion to be identified or outcome to be predicted accurately. Recently, radiomics, a newly emerging form of imaging analysis that extracts relevant features from large-scale imaging data, has shown an advantage to offer improved diagnostic, prognostic, and predictive accuracy as compared to conventional radiographic approaches (22–24). However, the use of radiomics as clinical biomarkers still necessitates evidence supports, and the method of which still necessitates amelioration to achieve routine clinical adoption. Its prospective aspect in the evaluation of gastric diseases is still unclear.

Therefore, the purpose of this study was to develop a computational-assisted approach that relies primarily on large-scale radiographic-radiomic (RR) features from contrast-enhanced CT images, with the aim to elaborate on this quantitative approach could help decipher histopathological characteristics of GCs and predict patients' postoperative outcomes.

MATERIALS AND METHODS

Patients

This was a retrospective study involving routine at a single medical center. Ethics committee approval was granted by local institutional ethics review board with a waiver of written informed consent. All procedures performed in studies involving human participants were in accordance with the 1964 Helsinki Declaration and its later amendments.

We queried our institution's medical database to derive all histologically proved cases of GCs between January 2014 and December 2016. A total of 783 histologically proved cases of GCs were identified in this query. Among all patients, we included patients who fulfilled the following criteria: (i) patients who had preoperative CT images with optimal gastric distension; (ii) patients whose primary gastric lesion was detectable on CT images; and (iii) patients who underwent standard gastrectomy and without the history of preoperative chemoradiation therapy. Thereafter, a total of 554 consecutive patients were identified and comprised the primary cohort according to the patient recruitment pathway as well as the inclusion and exclusion criteria listed in supplemental data (see Figure S1, Supplementary Digital Content, http://links.lww.com/CTG/A94). Median time interval between CT examination and surgery was 9 days (range, 6–14 days).

CT image acquisition

For all examinations, a 128-slice CT scanner was used (SOMATOM; Definition AS$^+$, Siemens, Forchheim, Germany). The CT scans, covering from the liver to the hypogastric region, were acquired during a breath-hold with the patient supine. The detail parameters and imaging methodologies were summarized in supplemental data (S-text-1, see Supplementary Digital Content, http://links.lww.com/CTG/A94).

Surgical procedure and histopathological classification

All patients underwent primary gastrectomy with regional lymph node (LN) dissection according to the Japanese GC treatment guidelines 2010 (25). The perigastric LNs (N1), the LNs along the left gastric, common hepatic, celiac, and splenic arteries, and those at the splenic hilum (N2) were systematically dissected, regardless of their appearance on the CT images. LNs in the hepatoduodenal ligament, retropancreatic artery, mesenteric artery, midcolic artery, and para-aortic regions (N3/N4) were dissected if they were visible and palpable at surgery. Node packets were sent separately for microscopic examination for the presence of metastasis.

Postoperative histopathological specimens and node packets were analyzed by pathologists within the same academic institution with subspecialty training in gastrointestinal (GI) pathology. Histopathological variables included the pT stage (pT1–pT4), pN stage (pN0–pN4), Lauren & Borrmann (L&B) classification, WHO classification, and absence or presence of LVI. Pathological stage was assessed according to the eighth American Joint Committee on Cancer (AJCC) staging system (26).

Prognostic association of histopathologic status of GCs with overall survival (OS) was demonstrated in previous studies (7,9,12,13,15). Thus, in the current study, the histopathological status was scaled by: (i) pT1-2 stage (0 score) vs pT3-4 stage (1 score); (ii) pN0 stage (0 score) vs pN+ stage (1 score); (iii) low-L&B stage (0 score, intestinal types and Borrmann types I–III) vs high-L&B stage (diffuse type or Borrmann type IV) grade; (iv) low-WHO grade (0 score, papillary carcinoma or high differentiated tubular adenocarcinoma) vs high-WHO grade (1 score, medium differentiated tubular adenocarcinoma or poorly differentiated tubular adenocarcinoma or mucinous adenocarcinoma or signet ring cell carcinoma); and (v) LVI− (0 score) vs LVI+ (1 score). Finally, an overall histopathological score (H-score), representing the disease's overall aggressiveness, was derived by summing all status scores at each histopathological subtype. Patients were classified into low-H-score (0–3) and high-H-score (4–5) category, respectively. Adverse histopathological

status (AHS) was those with higher pT stage, higher pN stage, higher L&B grade, higher WHO grade, LVI+, or higher H-score.

Follow-up

After curative surgery, all patients were followed up with intervals of 3–6 months on the base of imaging examinations and were censored at the time of recurrence, death, emigration, or December 31, 2018, whichever came first.

Radiographic evaluation

All CT images were retrospectively interpreted by 2 radiologists (C.L. and L.Q.) who had 3-year (C.L.) and 10-year (L.Q.) experience in reading GI images. Both the readers were members of the institution's GI disease management team and had read >500 GI CT studies.

Our radiographic evaluation, referring to the methods previously reported (18,26–28), included several structured imaging features of GCs as follows: (i) region of tumor involvement (cardia, fundus, body, or antrum); (ii) maximum length of the tumor (L-max); (iii) tumor margin (sharply defined and ill defined); (iv) tumor growth pattern (intramural, extramural, transmural, diffusive, or invasive); (v) intratumor necrosis (absent or present); (vi) tumor ulceration (absent or present); (vii) serosal invasion (absent or present), wherein the serosal invasion was defined as an irregular or nodular outer margin of the serosal layer and/or a dense band-like perigastric fat infiltration (8,13) and blurry perigastric fat space (absent or present); (viii) radiographic T stage (rT1, rT2, rT3, and rT4); (ix) tumor arterial enhancement (TAE), which measured the CT Hounsfield unit at the target region; (x) tumor parenchymal enhancement (TPE); (xi) the tumor contrast between arterial and parenchymal enhancement (CAP); and (xii) the short axis length of the largest LN discernible (LND) was individually determined, and LNDs of less than 5 mm were rounded down to 0 mm.

All cases were scored individually first and then reviewed together by 2 readers 2 weeks after individual evaluation. Any disagreement at informed consent between the readers was discussed until a final standard consensus was generated. Individual scores were designated for the calculation of interobserver agreement. Consenting scores were used for classification performance. The measurable radiographic features such as L-max, LND, TAE, TPE, and CAP were averaged between the 2 radiologists.

Radiomic features

In the next step, 2 radiologist residents (Q.L., reader #3; and Q.-X.F., reader #4) who were not involved in the abovementioned radiographic interpretation analysis were asked for radiomic analysis. Lesion segmentation was semiautomatically performed with a dedicated commercial software package (Frontier, Syngo via, Siemens healthcare), wherein a user-defined region of interest was contoured by the radiologist to initially overlay the lesion and perinormal tissue, then a dichotomic classification algorithm was used to automatically segment the tumor from perinormal lesion step by step (Figure 1).

After lesion segmentation, imaging features were analyzed from target volumes using an open-source python package for the extraction of radiomic features (https://pyradiomics.readthedocs.io/en/latest/#) (23). Image normalization was performed using a method that remaps the histogram to fit within $\mu \pm 3\sigma$ (μ: gray-level mean between the volumetric interest and σ: gray-level SD). A total of 1,210 radiomic features were computed for target volume based on the following 9 texture analysis methods available in the software package: (i) 19 features of first-order intensity; (ii) 13 features of shape; (iii) 16 features of gray-level size zone matrix (GLSZM); (iv) 16 features of run-length matrices; (v) 5 features of neighborhood gray-tone difference matrix; (vi) 14 features of gray-level difference matrix; (vii) 23 features of gray-level co-occurrence matrix; (viii) 368 features of log-sigma 2, 3, 4, and 5 mm; and (ix) 736 features of wavelets. The extracted radiomic features were normalized to a standard unit with 0 center using the following equation:

$$\overrightarrow{x_n}\text{normalized} = \frac{\overrightarrow{x_n} - \overline{x_n}}{\sqrt{{x_{1n}}^2 + {x_{2n}}^2 + \ldots + {x_{mn}}^2}}, \quad (1)$$

where $\overrightarrow{x_n}$ is the value of feature N, and $\overline{x_n}$ is the average value of all features.

To evaluate intraobserver reliability, reader #3 repeated the feature extraction twice in a 1-week period. Reader #4 completed the remaining image segmentations, and the readout sessions were conducted over a period of 2 months. The reliability was calculated by using intraclass correlation coefficient (ICC). Radiomic features with both intraobserver and interobserver ICC values greater than 0.9 (indicating excellent stability) were selected for subsequent investigation.

AHS-related R-scores

Six R-scores related to pT stage, pN stage, L&B classification, WHO grade, LVI status, and H-score were developed, respectively. Data were randomly designated training/validation (n = 370) and test (n = 184) group, respectively. The test data set helped test the accuracy of model conducted from training data.

Reducing the feature space dimension aims to discard uninformative characteristics, prevent overfitting, speed up the learning process, and improve the model's interpretability. A least absolute shrinkage and selection operator (Lasso) logistic regression algorithm, with penalty parameter tuning conducted by 10-fold cross-validation, was then applied to select AHS-related radiomic features with nonzero coefficients from the primary training cohort. The R-score was generated through a linear combination of selected features weighted by their respective coefficients as depicted in equation 1:

$$Y = intercept + \sum_{i=1}^{n} \beta_i \times log(x_i) \quad (2)$$

where Y is the output, β_i is the nonzero coefficient, and x_i is the variable selected by Lasso analysis.

Development, performance, and validation of predictive models

Univariate and multivariate regression analyses were used to develop the risk models, namely RR model, for predicting AHS in the primary cohort of training set. Candidate variables were age, sex, 13 consenting radiographic features, and 6 developed R-scores. Variables at univariate analyses at a significant level were candidates for stepwise multivariate analysis. Predictive model was formulated based on the results of multivariate regression analysis. The model is based on proportionally converting each regression coefficient in multivariate logistic regression to a 0- to 100-point scale. The effect of the variable with the highest β coefficient (absolute value) is assigned 100 points. The points are added across independent variables to derive total points, which are converted to predicted probabilities (Pi).

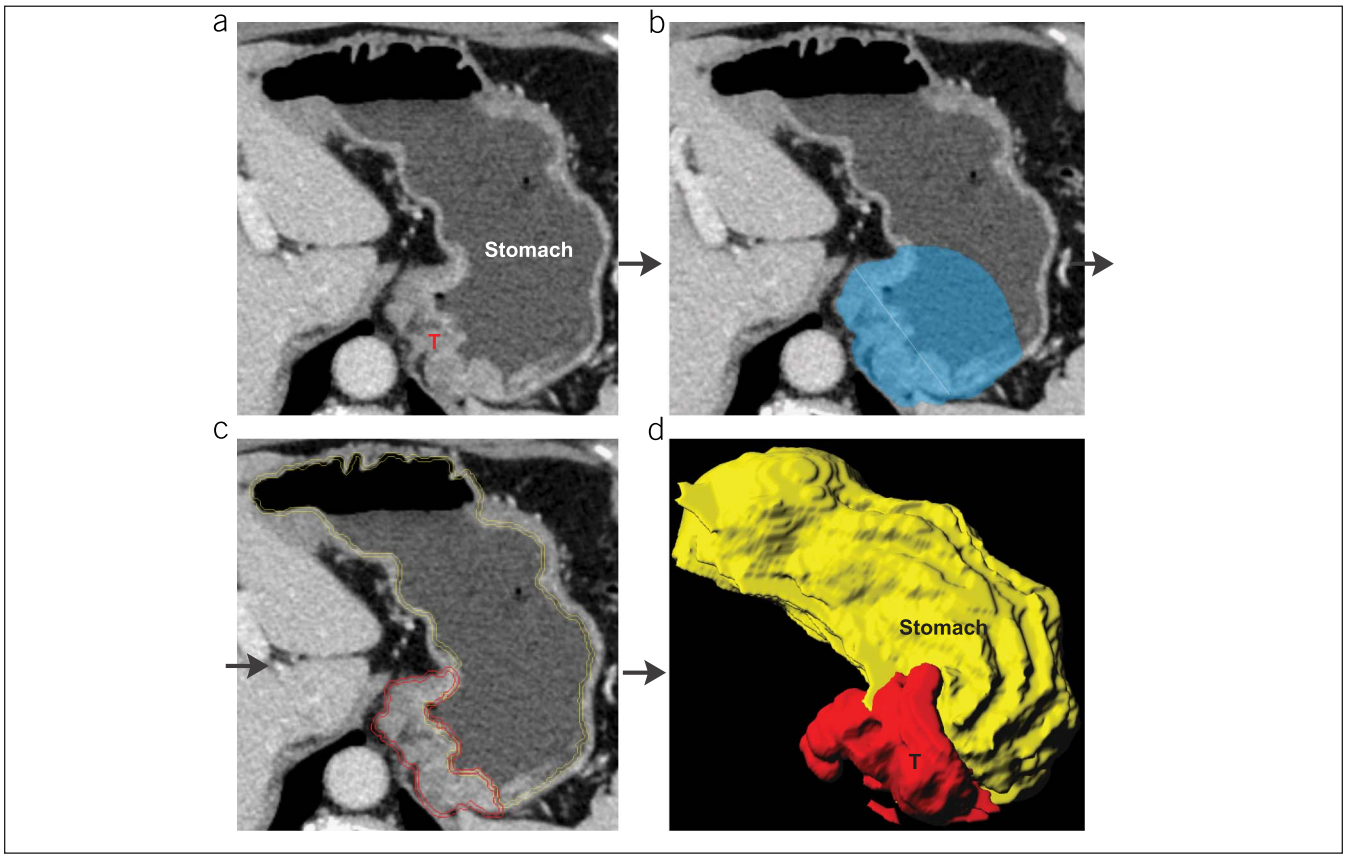

Figure 1. Stepwise segmentation of GC with a Frontier software package on Syngo via workstation: First, radiologists manually draw a seed region that encloses the contour of tumor and adjacent tissues on the target volume (**a**–**b**), then tumor contour was semiautomatically segmented slice by slice with dedicated algorithms and a hand-craft approach, followed by an entire volumetric interest (VOI) (**c**) and a 3-dimensional view (**d**) of the tumor were determined. GC, gastric cancer.

Statistical analysis

Categorical variables were compared by using the χ^2 test or Fisher exact test. Continuous variables were compared by using the Student *t* test or Mann-Whitney *U* test, when appropriate.

The discrimination performance of established models was quantified by the receiver operating characteristic curve and area under the curve (AUC) value. The performance of the RR models was internally validated in an independent test set by using the formula derived from the primary cohort.

OS was computed from the date of surgery to the date of death or censored at the date of last follow-up. Recurrence-free survival (RFS) was defined as the interval between surgery and radiographic detection of recurrence, last follow-up, or death. Survival curves were generated by using the Kaplan-Meier method and compared by 2-sided log-rank tests. Univariable and multivariable analyses with Cox proportional hazards regression determined predictors of disease-specific recurrence and disease-specific mortality. Variables that reached statistical significance at the univariable analysis were considered for the multivariable model. Statistical analysis was performed by using R software (version 3.4.4, R Project for Statistical Computing, www.r-project.org). A 2-sided *P* value less than 0.05 was considered to indicate statistical significance.

RESULTS

Table 1 describes the characteristics of the analysis cohort. The prevalence of high-pT stage, pN+ stage, high-L&B classification, high-WHO grade, and LVI+ was 60.1% (333/554), 60.5% (335/554), 55.2% (306/554), 78.9% (437/554), and 51.6% (286/554), respectively, according to the histopathological definition. The overall histopathological score was low H-score in 52% (288/554) and high H-score in 48.0% (266/554), respectively. The detailed histopathological results of nodal packages resected at surgery were summarized in supplemental data (see Table S1, Supplementary Digital Content, http://links.lww.com/CTG/A94).

Radiographic findings

The results of radiographic evaluation are summarized in Table 2. The interobserver agreement was good for reporting gastric cardia involvement, L-max, intramural growth, radiographic T stage, TAE, TPE, and CAP measurement, wherein the kappa or ICC ranges from 0.65 to 0.88. The agreement was intermediate for reporting gastric fundus, body and antrum involvement, extramural and transmural growth, necrosis, ulceration, blurry fat space, and N stage, wherein the coefficient ranges from 0.40 to 0.59. The agreement was relatively poor for defining the margin, diffuse and invasive growth, and peritoneal seeding sign of the tumor, wherein the coefficient ranges from 0.29 to 0.39.

With the Spearman or Pearson correlation test, 21 radiographic features were associated with pT stage and pN status

Table 1. Clinicopathologic characteristics in training and test groups

Imaging findings	Training (n = 370)	Test (n = 184)	*P*
N (%)	66.8	33.2	0.206
Age, n (%)	—	—	0.200
≤60 yr	164/370 (44.3)	86/184 (46.7)	—
>60 yr	206/370 (55.7)	98/184 (53.3)	—
Sex	—	—	0.043
Male	276/370 (74.6)	135/184 (73.4)	—
Female	94/370 (25.4)	49/184 (26.6)	—
Eighth AJCC stage (c-TNM), n (%)	—	—	0.713
I	64/370 (17.3)	39/184 (21.2)	—
II	75/370 (20.3)	41/184 (22.3)	—
III	231/370 (62.4)	104/184 (56.5)	—
Treatment, n (%)	—	—	0.941
Gastrectomy	145/370 (39.2)	73/184 (39.7)	—
Gastrectomy + adjuvant therapy	225/370 (60.8)	111/184 (60.3)	—
Pathological T stage, n (%)	—	—	0.955
pT1 stage	102/370 (27.6)	54/184 (29.3)	—
pT2 stage	45/370 (12.2)	20/184 (10.9)	—
pT3 stage	70/370 (18.9)	34/184 (18.5)	—
pT4 stage	153/370 (41.3)	76/184 (41.3)	—
Pathological N stage, n (%)	—	—	0.539
pN0 stage	146/370 (39.5)	73/184 (39.7)	—
pN1 stage	55/370 (14.9)	24/184 (13.0)	—
pN2 stage	57/370 (15.4)	27/184 (14.7)	—
pN3a stage	70/370 (18.9)	30/184 (16.3)	—
pN3b stage	42/370 (11.3)	30/184 (16.3)	—
Histopathologic type			
WHO score, median (range)[a]	2.5 (3)	2.5 (3)	0.617
Lauren score, median (range)[a]	1 (1)	1 (1)	0.872
Borrmann score, median (range)[a]	0 (1)	0 (1)	0.988
LVI, n (%)	193/370 (52.2)	93/184 (50.5)	0.788
H-score, n (%)	—	—	0.769
Score 0–3	192/370 (51.9)	96/184 (52.2)	—
Score 4–5	178/370 (48.1)	88/184 (47.8)	—

Values are no. of findings, and values in parentheses are percentages, unless indicated otherwise.
AJCC, American Joint Committee on Cancer; H-score, histopathologic score; LVI, lymphatic vascular infiltration; WHO, World Health Organization.
[a]Reports are median and range. The pT and pN stages are based on the WHO for Gastric Cancer Guidelines.

(correlation coefficients 0.09–0.66, $P < 0.05$), 12 radiographic features were associated with L&B classification (correlation coefficients 0.09–0.19, $P < 0.05$), 9 radiographic features were associated with WHO grade (correlation coefficients 0.11–0.17, $P < 0.05$), 18 radiographic features were associated with LVI (correlation coefficients 0.05–0.32, $P < 0.05$), and 18 radiographic features were associated with H-score (correlation coefficients 0.12–0.43, $P < 0.05$). Among all features, L-max and radiographic T stage were 2 strong predictors of AHS.

AHS-related R-scores

The results of radiomic analysis are summarized in Table 3. Lasso regression model selected 26 pT-related features, 71 pN-related features, 85 L&B-related features, 39 WHO grade–related features, 89 LVI-related features, and 75 H-score–related features, respectively, on the basis of the primary training cohort (see Figure S2, Supplementary Digital Content, http://links.lww.com/CTG/A94). The R-score was then generated through a linear combination of selected feature weights by their respective coefficients using the formula depicted in equation 1. The AUCs of

Table 2. Radiographic findings and correlation tests with AHS of GC

Radiographic finding	Kappa value	Training (n = 370)	Test (n = 184)	Correlation coefficient					
				pT stage	pN stage	LVI status	L&B grade	WHO grade	H-score
Zone involved									
Cardia	0.75 (0.69–0.81)	122/370 (33.0)	62/184 (33.7)	0.22[d]	0.11[c]	0.10[c]	0.09[c]	0.07	0.17[d]
Fundus	0.42 (0.28–0.55)	46/370 (12.4)	26/184 (14.1)	0.24[d]	0.17[d]	0.06	0.02	0.12[d]	0.16[d]
Body	0.53 (0.46–0.60)	247/370 (66.8)	109/184 (59.2)	0.28[d]	0.18[d]	0.13[d]	0.09[c]	0.05	0.18[c]
Antrum	0.59 (0.53–0.66)	208/370 (56.2)	98/184 (53.3)	−0.22[d]	−0.09[c]	−0.04	−0.06	−0.04	−0.10
L-max, cm[a]	0.88 (0.86–0.90)	4.68 ± 2.26	2.7 ± 2.17	0.63[d]	0.48[d]	0.32[d]	0.19[d]	0.17[d]	0.43[d]
Tumor margin (ill defined)	0.35 (0.29–0.42)	235/370 (63.5)	120/184 (65.2)	0.35[d]	0.33[d]	0.18[d]	0.08[d]	0.12[d]	0.28[d]
Tumor growth pattern									
Intramural	0.67 (0.23–0.98)	370/370 (100)	182/184 (98.9)	−0.05	−0.05	0.00	0.01	−0.03	0.01
Extramural	0.45 (0.32–0.58)	46/370 (12.4)	20/184 (10.9)	0.28[d]	0.25[d]	0.11[c]	0.11[c]	0.05	0.17[d]
Transmural	0.40 (0.27–0.53)	46/370 (12.4)	19/184 (10.3)	0.26[d]	0.24[d]	0.15[d]	0.09[c]	0.04	0.16[d]
Diffusive	0.38 (0.27–0.50)	72/370 (19.5)	30/184 (16.3)	0.31[d]	0.27[d]	0.20[d]	0.11[d]	0.06	0.20[d]
Invasive	0.39 (0.30–0.48)	138/370 (37.3)	59/184 (32.1)	0.50[d]	0.35[d]	0.01	0.13[d]	0.14[d]	0.28[d]
Intratumoral necrosis	0.42 (0.10–0.75)	7/370 (1.9)	4/184 (2.1)	0.06	0.04	0.08	0.02	0.07	0.04
Intratumoral ulcer	0.47 (0.40–0.53)	246/370 (66.5)	117/184 (63.6)	0.32[d]	0.27[d]	0.11[c]	0.03	0.08	0.16[d]
Blurry fat space	0.46 (0.36–0.56)	87/370 (23.5)	38/184 (20.7)	0.28[d]	0.30[d]	0.11[c]	0.07	0.08	0.14[d]
Peritoneal seeding sign	0.29 (0.12–0.47)	26/370 (7.0)	12/184 (6.5)	0.27[d]	0.18[d]	0.05[c]	0.03	0.07	0.08
Radiographic T stage[b]	0.65 (0.60–0.70)			0.66[d]	0.50[d]	0.26[d]	0.15[d]	0.15[d]	0.35[d]
rT1-2		116/370 (31.4)	60/184 (32.6)						
rT3-4		154/370 (41.6)	124/184 (67.4)						
Radiographic N status[b]									
rN1 stage (stations 1–6)	0.57 (0.50–0.64)	274/370 (74.1)	131/184 (71.2)	0.45[d]	0.45[d]	0.20[d]	0.11[d]	0.11[d]	0.26[d]
rN2 stage (stations 7–11)	0.59 (0.52–0.66)	135/370 (36.5)	66/184 (35.9)	0.36[d]	0.35[d]	0.15[d]	0.09[c]	0.09[c]	0.19[d]
rN3 stage (stations 12–14)	0.47 (0.34–0.61)	45/370 (12.2)	19/184 (10.3)	0.22[d]	0.20[d]	0.13[d]	0.06	0.02	0.11[c]
rN4 stage (stations 15 and 16)	0.57 (0.44–0.69)	45/370 (12.2)	18/184 (9.8)	0.12[d]	0.21[d]	0.12[d]	0.06	0.03	0.08
LND, cm[a]	0.74 (0.69–0.78)	0.62 ± 0.62	0.61 ± 0.67	0.48[d]	0.52[d]	0.15[d]	0.10[c]	0.11[d]	0.26[d]
TAE[a]	0.85 (0.82–0.87)	1.12 ± 0.28	1.09 ± 0.25	0.27[d]	0.17[d]	0.12[d]	0.04	0.03	0.12[d]
TPE[a]	0.84 (0.81–0.86)	1.23 ± 0.27	1.21 ± 0.28	0.36[d]	0.19[d]	0.13[d]	0.04	0.09[c]	0.14[d]
CAP[a]	0.84 (0.81–0.87)	0.92 ± 0.16	0.91 ± 0.18	−0.09[c]	−0.03	0.01	−0.01	0.01	0.04

Values are no. of findings, and values in parentheses are percentages, unless indicated otherwise.
Continuous data are analyzed by the *t* test, and counted data are analyzed by χ^2 tests.
AHS, adverse histopathological status; CAP, tumor contrast between arterial and parenchymal enhancement; GC, gastric cancer; H-score, histopathological score; L&B grade, Lauren & Borrmann grade; L-max, maximum length of the tumor; LND, the short axis diameter of the largest lymph nodes discernible; LVI, lymphatic vascular infiltration; TAE, arterial enhancement of the tumor; TPE, parenchymal enhancement of the tumor; WHO, World Health Organization.
[a]Reports are mean and SD.
[b]Radiographic T and N status are based on Japanese Research Society for Gastric Cancer Guidelines.
[c]*p*-value < 0.05.
[d]*p*-value < 0.01.

Table 3. Top-ranked radiomic features and AHS-related R-scores with Lasso analysis

Status	Features selected	Top 3 features	R-score			AUC	
			AHS$^-$	AHS$^+$	*P*	Training	Test
pT	26	(1) Wavelet-HLL first-order mean; (2) original GLRLM long run emphasis; and (3) log-sigma-3-0-mm 3D GLSZM gray-level variance	0.33 (0.28)	0.79 (0.21)	<0.001	0.88 (0.86–0.91)	0.87 (0.84–0.90)
pN	71	(1) Log-sigma-4-0-mm-3D GLSZM gray-level variance; (2) wavelet-HLH GLRLM short run high gray-level emphasis; and (3) wavelet-HLL first-order mean	0.46 (0.24)	0.69 (0.21)	<0.001	0.75 (0.71–0.79)	0.73 (0.70–0.77)
L&B	85	(1) Log-sigma-5-0-mm-3D GLRLM run variance; (2) log-sigma-2-0-mm 3D GLSZM gray-level variance; and (3) wavelet-HLH GLCM cluster prominence	0.48 (0.17)	0.55 (0.18)	<0.001	0.62 (0.57–0.65)	0.61 (0.55–0.64)
WHO	39	(1) Wavelet-HHL GLSZM zone entropy; (2) wavelet-HHL GLSZM gray-level variance; and (3) wavelet-LHH first-order mean	0.74 (0.11)	0.81 (0.11)	<0.001	0.65 (0.61–0.69)	0.63 (0.59–0.67)
LVI	89	(1) Wavelet-LLH GLSZM gray-level variance; (2) wavelet-HLH NGTDM complexity; and (3) log-sigma-5-0-mm-3D GLSZM zone entropy	0.45 (0.17)	0.58 (0.16)	<0.001	0.69 (0.65–0.72)	0.68 (0.64–0.71)
H-score	75	(1) Log-sigma-5-0-mm-3D GLSZM zone entropy; (2) log-sigma-4-0-mm-3D GLSZM gray-level variance; and (3) wavelet-HLL first-order mean	0.41 (0.20)	0.74 (0.25)	<0.001	0.79 (0.74–0.82)	0.78 (0.73–0.80)

AHS, adverse histopathological status; AUC, area under the curve of ROC analysis; H-score, histopathologic score; L&B grade, Lauren & Borrmann grade; LVI, lymphatic vascular infiltration; ROC, receiver operating characteristic; WHO, World Health Organization.

R-scores in test set were very close to those of training set, suggesting good reproducibility of the newly developed radiomic signatures in internal validation.

RR classification models

pT status. R-score (odds ratio [OR], 45.6; 95% confidence intervals [CIs], 14.4–143.9, $P < 0.001$), TAE (OR, 7.78; 95% CIs, 2.09–28.9, $P = 0.002$), TPE (>0.42; OR, 0.002; 95% CIs, 0–0.022, $P < 0.001$), rT stage (OR, 3.60; 95% CIs, 2.29–5.65, $P < 0.001$), and L-max (OR, 1.32; 95% CIs, 0.94–3.19, $P = 0.007$) were the independent predictors of pT status. The classification model was formed: $Y = -2.87 + 3.82 \times$ R-score $+ 2.05 \times$ TAE $- 6.38 \times$ TPE $+ 1.28 \times$ rT stage $+ 0.27 \times$ L-max. The resulting classification model demonstrated good accuracy in discriminating the low- from the high-pT stage, with an AUC of 0.93 (95% CI, 0.92–0.94) in training and 0.94 (95 CI, 0.92–0.95) in test data (Figure 2a).

pN status. R-score (OR, 4.26; 95% CIs, 1.44–12.6, $P = 0.009$), LND (OR, 4.80; 95% CIs, 2.69–8.59, $P < 0.001$), rT stage (OR, 1.54; 95% CIs, 1.12–2.12, $P = 0.008$), L-max (OR, 1.15; 95% CIs, 0.98–1.34, $P = 0.047$), and blurry fat space (OR, 2.12; 95% CIs, 1.09–4.11, $P = 0.026$) were the independent predictors of pN status. The classification model was formed: $Y = -3.13 + 1.45 \times$ R-score $+ 1.57 \times$ LND $+ 0.43 \times$ rT stage $+ 0.14 \times$ L-max $+ 0.75 \times$ blurry fat space. The model demonstrated good accuracy in discriminating pN+ from pN0, with an AUC of 0.85 (95% CI, 0.82–0.86) in training and 0.83 (95% CI, 0.80–0.85) in test data (Figure 2b).

L&B grade. R-score (OR, 6.93; 95% CIs, 1.43–33.5, $P = 0.016$) and L-max (OR, 1.12; 95% CIs, 1.01–1.23, $P = 0.023$) were the independent predictors of L&B-related status. The classification model was formed: $Y = -1.36 + 1.94 \times$ R-score $+ 0.11 \times$ L-max, demonstrating with an AUC of 0.63 (95% CI, 0.59–0.65) in training and 0.59 (95% CI, 0.55–0.63) in test data for discriminating the low- from the high-L&B grade (Figure 2c).

WHO grade. R-score (OR, 60.8; 95% CIs, 9.54–387.5, $P < 0.001$) and diffusive growth pattern (OR, 2.52; 95% CIs, 1.05–6.04, $P = 0.039$) were the independent predictors of WHO grade. The classification model was formed: $Y = -1.95 + 4.11 \times$ R-score $+ 0.92 \times$ diffusive growth, with an AUC of 0.66 (95% CI, 0.63–0.68) in training and 0.63 (95% CI, 0.61–0.64) in test data for discriminating the low- from the high-WHO grade (Figure 2d).

LVI status. R-score (OR, 15.6; 95% CIs, 4.32–56.2, $P < 0.001$) and L-max (OR, 1.17; 95% CIs, 1.05–1.30, $P = 0.005$) were the independent predictors of LVI status. The classification model was formed: $Y = -2.06 + 2.74 \times$ R-score $+ 0.15 \times$ L-max, with an AUC of 0.71 (95% CI, 0.68–0.73) in training and 0.69 (95% CI, 0.67–0.71) in test data for discriminating LVI+ from LVI− (Figure 2e).

H-score. R-score (OR, 7.19; 95% CIs, 4.27–12.1, $P < 0.001$), tumor margin (OR, 1.65; 95% CIs, 1.06–2.58, $P = 0.028$), and L-max (OR, 1.15; 95% CIs, 1.03–1.28, $P = 0.016$) were the independent predictors of H-score. The classification model was formed: $Y = -3.32 + 1.97 \times$ R-score $+ 0.50 \times$ tumor margin $+$

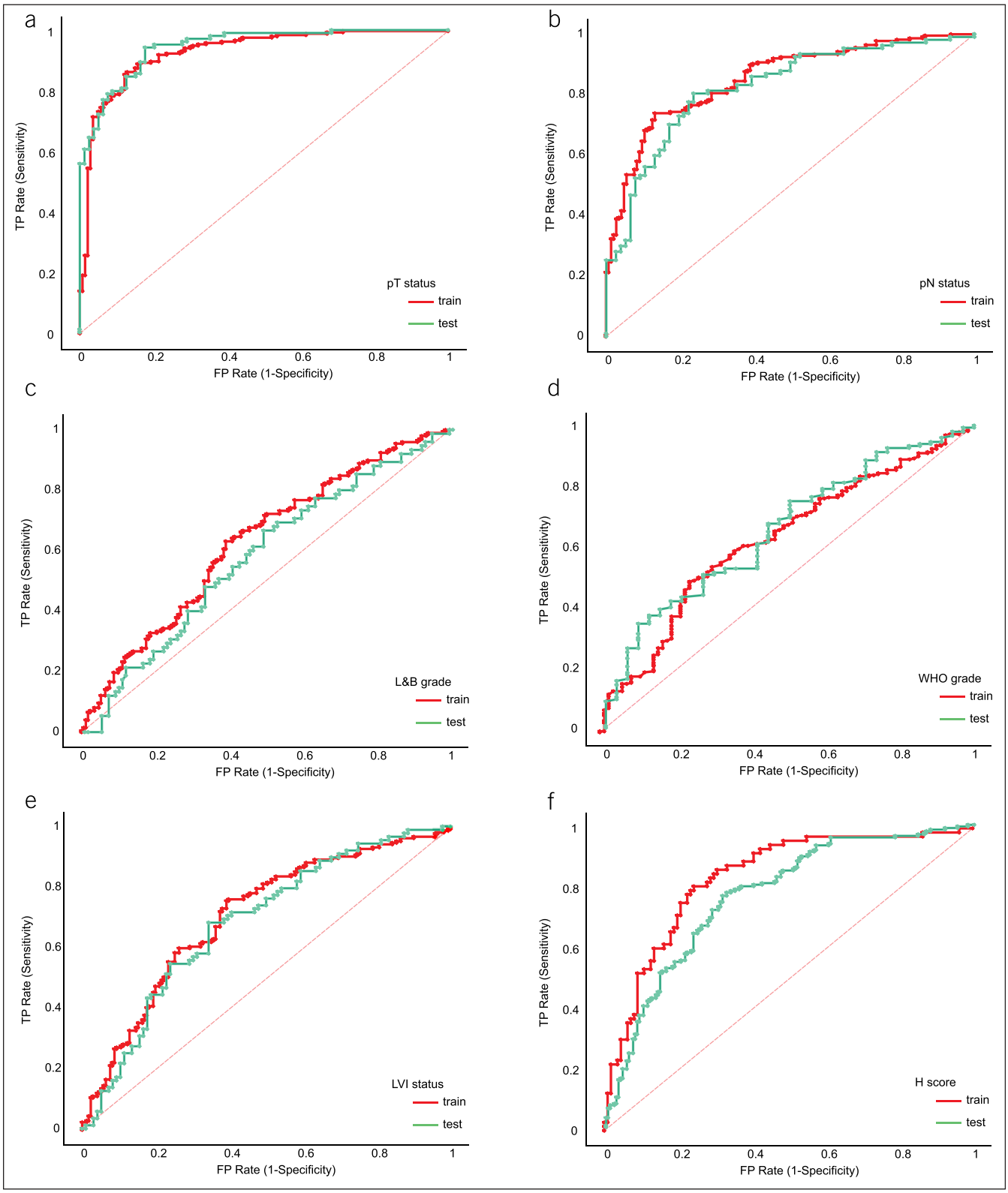

Figure 2. The ROC curves of RR classification models for predicting adverse histopathological status (AHS) in training and test set: (**a**) The areas under the ROC curves representing the satisfactory results can be achieved in discriminating the low- from the high-pT stage. Keys in (**a**) are the same for (**b**) pN status, (**c**) L&B grade, (**d**) WHO grade, (**e**) LVI status, and (**f**) H-score. FP, false positive; H-score, histopathologic score; L&B grade, Lauren & Borrmann grade; LVI, lymphatic vascular infiltration; TP, true positive; ROC, receiver operating characteristic; RR, radiographic-radiomic; WHO, World Health Organization.

0.14 × L-max, with an AUC of 0.84 (95% CI, 0.81–0.86) in training and 0.77 (95% CI, 0.75–0.79) in test data for discriminating the low- from the high-H-score (Figure 2f).

Validation of RR models

The predictive models were tested in the validation cohort. Using an optimal threshold that maximizes the Youden index of ROC analysis from training data, the diagnostic performance of 6 RR predictive models was summarized in Table 4.

Preoperative predictors of survival

As of December 2018, 428/554 patients (77.3%) were entirely followed up, and the remaining 126/554 patients (22.7%) were lost to follow-up. The recurrence rate for this cohort of patients (including censored data) was 28.5% (158/554); the overall death rate for this cohort of patients was 36.2% (147/554). The median RFS was 36 (95% CIs: 21.8–50.3) months; it was 41.2 (95% CIs: 30.8–51.7) months for those with no evidence of recurrence and 16.5 (95% CIs: 5.2–27.8) months for those with recurrence. The median OS for all patients was 37.4 (95% CIs: 24.1–50.7) months; it was 41.2 (95% CIs: 30.8–51.6) months for those with no evidence of death and 18.9 (95% CIs: 7.5–30.3) months for those with death. The 1-year to 5-year RFS and OS status are summarized in lift tables in supplemental data (see Tables S2 and S3, Supplementary Digital Content, http://links.lww.com/CTG/A94).

The preoperative factors including age, sex, AJCC eighth stage (26), history of postoperative adjuvant therapy, radiologic features, and R-scores were integrated into a multivariate Cox model to determine the predictors associated with disease-specific recurrence and mortality of the patients after surgery. It demonstrated that higher L-max (OR, 1.11; 95% CI, 1.03–1.20; $P = 0.008$), presence of peritoneal seeding sign (OR, 1.87; 95% CI, 1.18–2.96; $P = 0.008$), higher R-score of pT (OR, 3.89; 95% CI, 2.22–6.79; $P < 0.001$), and higher R-score of pN (OR, 1.64; 95% CI, 1.04–2.57; $P = 0.032$) were the independent predictors of disease-specific recurrence. The older age (OR, 1.02; 95% CI, 1.00–1.19; $P = 0.009$), higher L-max (OR, 1.10; 95% CI, 1.01–1.19; $P = 0.022$), presence of peritoneal seeding sign (OR, 2.04; 95% CI, 1.28–3.26; $P = 0.003$), higher R-score of pT (OR, 3.96; 95% CI, 2.18–7.23; $P < 0.001$), and higher R-score of pN (OR, 1.96; 95% CI, 1.19–3.21; $P = 0.008$) were the independent predictors of disease-specific mortality. The AHS-based Cox model produced higher AUC (0.766; 95% CIs: 0.728–0.801) than the eighth AJCC staging model (0.653; 95% CIs: 0.611–0.692) for predicting disease-specific recurrence and produced higher AUC (0.778; 95% CIs: 0.742–0.812) than the eighth AJCC staging model (0.655; 95% CIs: 0.613–0.694) for predicting disease-specific mortality. The decision curve analysis (Figure 3) and Kaplan-Meier analysis (Figure 4) demonstrated that adding AHS-based scores to the AJCC staging model resulted in better net benefits and predictive abilities for stratifying recurrence and death risk of the patients after surgery.

Table 4. Diagnostic performance of RR models for AHS of GC

	Training			Test		
Classification	SEN	SPE	ACC	SEN	SPE	ACC
Low- vs high-pT	90.0%	78.6%	85.7%	94.2%	80.0%	88.0%
Low- vs high-pN	84.6%	64.3%	76.8%	83.3%	63.2%	75.0%
Low- vs high-L&B	73.7%	43.0%	59.5%	71.3%	40.0%	58.5%
Low- vs high-WHO	73.2%	44.5%	60.3%	72.8%	43.1%	59.4%
LVI- vs LVI+	67.2%	62.8%	65.1%	76.4%	50.0%	62.7%
Low- vs high-H-score	78.1%	76.8%	77.3%	79.3%	63.8%	71.9%

ACC, accuracy; AHS, adverse histopathological status; AUC, area under the curve; GC, gastric cancer; H-score, histopathologic score; L&B grade, Lauren & Borrmann grade; LVI, lymphatic vascular infiltration; RR, radiographic-radiomic; SEN, sensitivity; SPE, specificity; WHO, World Health Organization.

DISCUSSION

This study was proposed to investigate prognostic aspects of integration between large-scale radiographic and radiomic features for preoperative individualized prediction of AHS and clinical outcomes in a cohort of 554 patients with GC. We report that CT radiomic features, converted into quantitative R-scores, can be the independent predictors of AHS. The risk model by integrating radiographic factors and R-scores can identify various types of AHS accurately. The model-computed AHS risk showed better discriminative ability than the eighth AJCC staging model in risk stratification, and the prognosis could be more accurately predicted by adding the AHS-based score to the eighth AJCC stage, which making us believe our research findings can play an important role and make a significant difference in the current clinical work of GC.

Clinically distinguishing the degree of pT and assessing the N stage are crucial for the clinical treatment protocols. Same with the previous study (3,18,19,28), we found that the accuracy of preoperative radiographic evaluation alone for detecting pT and pN stages was not satisfactory, while the computational model by integrating multiscale imaging factors had a great improvement in performance. R-score, TAE, TPE, rT stage, and L-max were the independent predictors of pT status, in which R-score was generated through 26 radiomic features derived from CT images. R-score, LND, rT stage, L-max, and blurry fat space were the independent predictors of pN status, in which R-score was generated through 71 radiomic features derived from CT images. In addition, Lasso analysis identified those features related to gray-level intensity, size, and inhomogeneity of the tumor were the primary components of R-scores, suggesting tumors with high pT and pN stages provided a larger size, a high degree of intratumoral heterogeneity, and a higher degree of TAE while a lower degree of TPE. In a study of 153 patients, researchers found that CT texture parameters, including the maximum frequency, mean, mode, and entropy, were correlated with pT and pN stages of GCs (29). Previous studies have shown that GLSZMs have shown better performance at capturing tumor heterogeneity than histogram-based features (23,24). Besides, our study included more samples, extracted more features, and had higher predictive accuracy for pT status. And importantly, our simple RR model, comprising 5 risk factors, could serve as an effective index to recognize pT and pN status, which can optimize the individualized treatment program and management of patients with GCs.

The predictive value of our RR model for L&B classification was not satisfactory. R-score and L-max were the independent predictors of L&B-related status, in which gray-level run-length

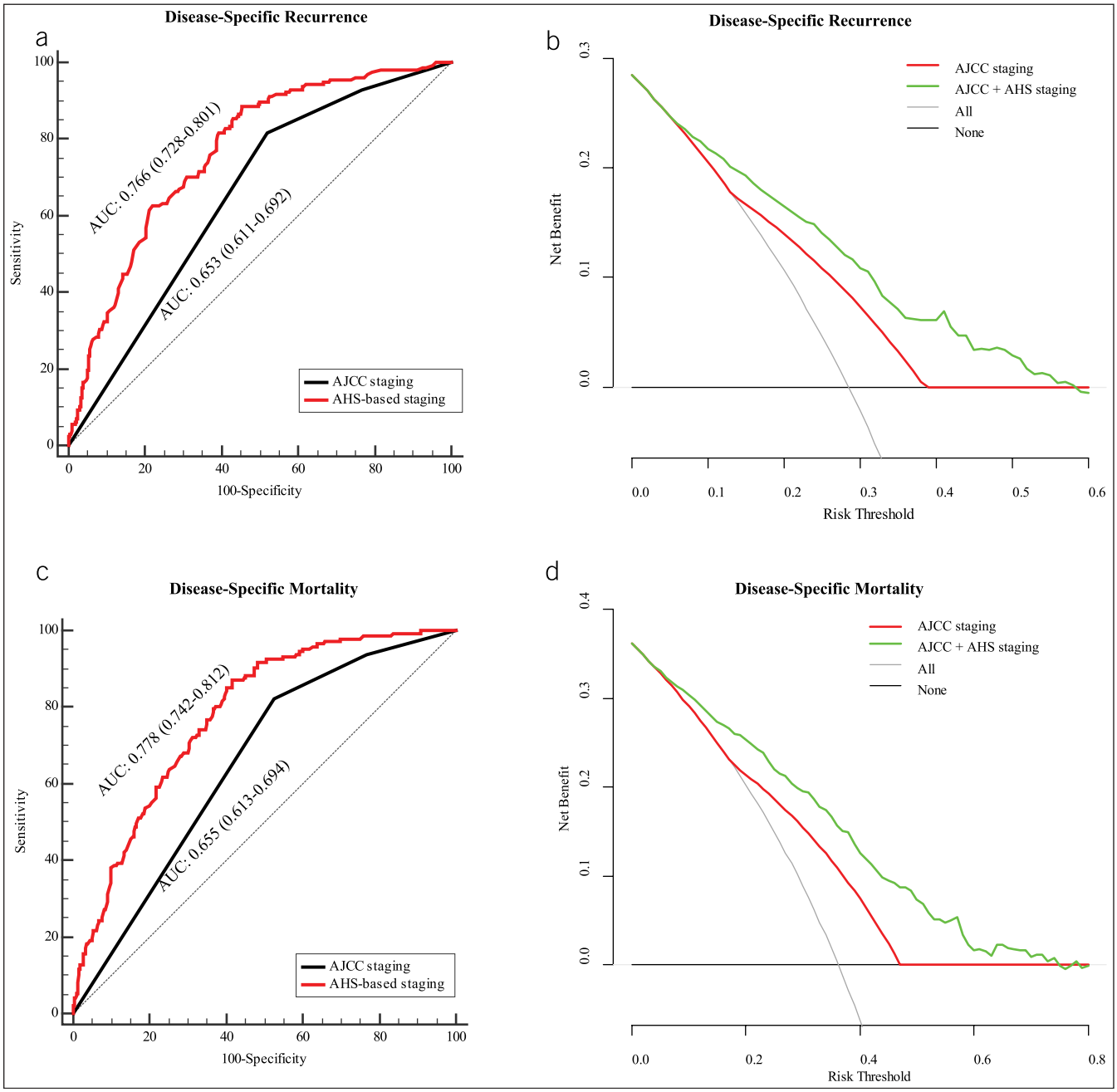

Figure 3. The ROC curves and decision curve analysis for each model: (**a**) ROCs between the AJCC staging model and AHS staging model for the prediction of disease-specific recurrence. (**b**) Decision curve and net benefit of the AJCC staging (red) vs AJCC + AHS staging model (green) for stratification of disease-specific recurrence. (**c**) ROCs between the AJCC and AHS staging model for the prediction of disease-specific mortality. (**d**) Decision curve and net benefit of the AJCC staging (red) vs AJCC + AHS staging model (green) for stratification of disease-specific mortality. AHS, adverse histopathological status; AJCC, American Joint Committee on Cancer; AUC, area under the curve; ROC, receiver operating characteristic.

matrix run variance, GLSZM gray-level variance, and wavelet-related cluster prominence were top-ranked radiomic features. These findings indicated that patients with diffuse type and Borrmann type IV have more vascular invasiveness, heterogeneity, and larger sizes, which makes the lesion more aggressive. Previous research studies have indicated that Borrmann type IV and diffuse type in GCs were associated with more advanced and unfavorable pathological features (7,12–14). However, few studies have reported the correlation of CT performance and Borrmann type IV/diffuse type in GCs, which makes it challenging to predict L&B grades based on radiographic characteristics. Liu et al. (21) found that CT texture analysis, especially the maximum attenuation, had a good effect in distinguishing the diffuse type of GC before surgery, whereas the study informed rarely used radiomic features, which may lead to a disappreciation of radiomic significance. Kim et al. (30) found that the accuracy of CT in diagnosing Borrmann type IV is 74.6%. However, the sample size in their study is small and the radiologists already

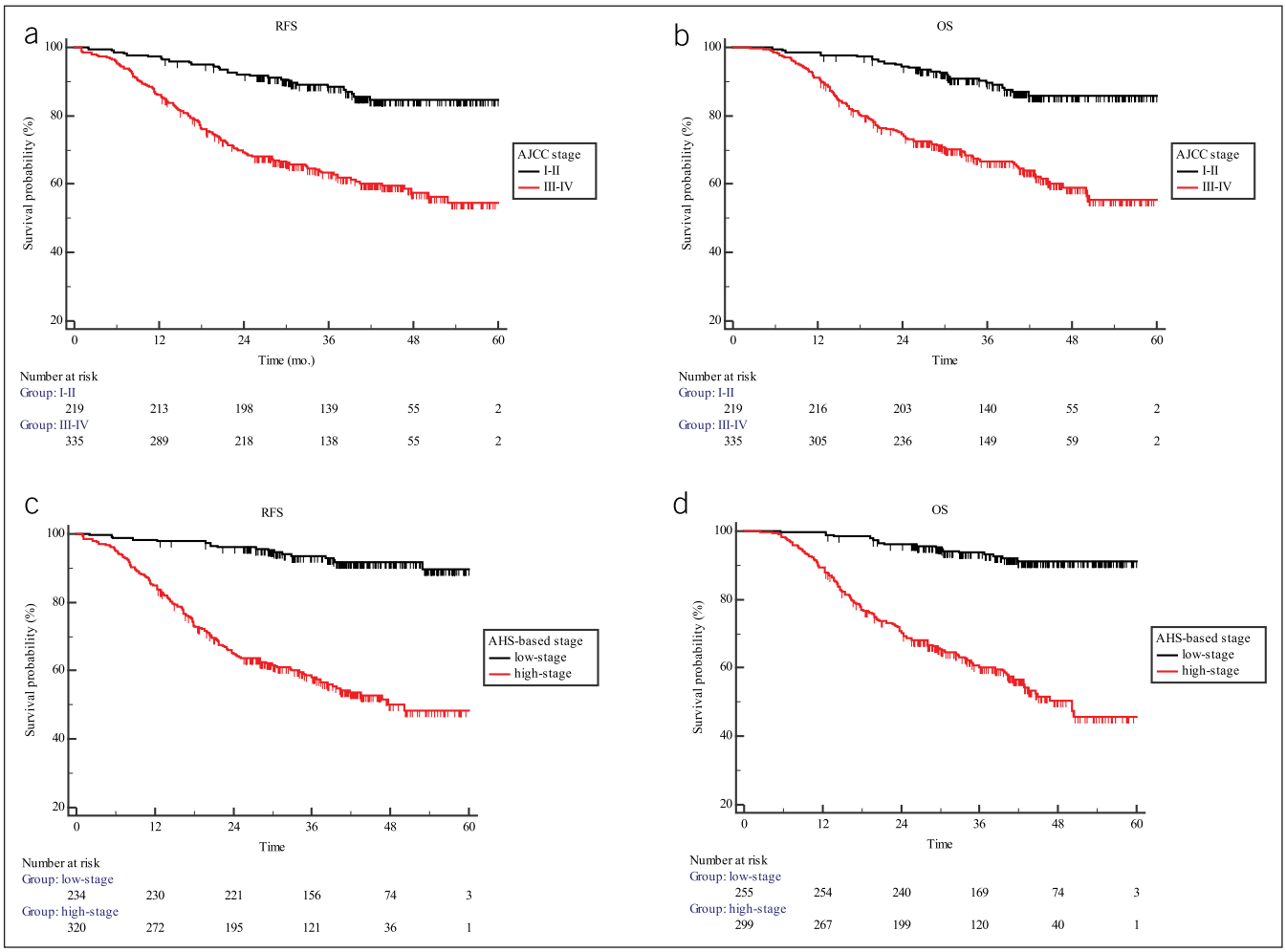

Figure 4. Kaplan-Meier survival curves of RFS and OS according to the eighth AJCC stage and AHS-based stage. (**a**) RFS stratified by the eighth AJCC stage. (**b**) OS stratified by the eighth AJCC stage. (**c**) RFS stratified by the AHS-based stage. (**d**) OS stratified by the AHS-based stage. The AHS-based stage widens the distance between the curves and better stratifies the recurrence and death probabilities. AJCC, American Joint Committee on Cancer; OS, overall survival; RFS, recurrence-free survival.

known the results of gastroscopy before interpreting the CT image, so the accuracy may be deviate.

Our data showed R-score formed by 39 radiomic features and diffusive growth pattern were the independent predictors of WHO grade, and the top 3 radiomic features were all related to wavelet, which indicated the high propensity for proliferation and tumor heterogeneity in medium and poorly differentiated carcinomas, signet ring cell carcinomas, and mucinous carcinomas. Li et al. (20) found that quantitative iodine concentration measurement using dual-phase–enhanced spectral CT examination is helpful to distinguish poorly differentiated GC from well-differentiated GC, while the radiation dose is higher than conventional CT that limited the current clinical applications. Nevertheless, we did not find study using radiomics to predict signet ring cell carcinomas in GCs. Taking a step forward, our approach might serve as alternative to assess WHO grade of GCs.

Our model was stable and reliable for detecting LVI preoperatively with an AUC of 0.71 in training and 0.69 in test data. R-score formed by 89 radiomic features and L-max were the independent predictors of LVI status. The top 3 radiomic features are wavelet-related gray-level variance, complexity, and log-sigma–related zone entropy. These results suggest that patients with LVI had a higher risk of intratumoral heterogeneity and neovascularization, which coincided with those reported in literatures. More evidences had confirmed the potential prognostic value of LVI in patients with GCs (7,15,16,31). However, few studies have reported the correlation of the CT and LVI status. Ma et al. (16) reported that tumor CT attenuation difference between noncontrast and portal and tumor-spleen attenuation difference in the portal phase are the independent predictors of LVI in GCs. However, the study involved only patients with advanced GC, which led to inevitable research bias. Therefore, it is urgent to establish a model suitable for patients at an early advanced stage.

Owing to the spatial and temporal heterogeneity of GCs, a single pathological state cannot accurately provide the complete histopathological characteristics of the tumor. Therefore, building a model noninvasively summing all histopathological status to extract biological information of tumors is an urgent need. The RR model shows a strong ability to stratify patients with GCs into low and high H-score groups with an AUC of 0.77–0.84, better than using L&B grade, WHO grade, and LVI status alone, which

can provide additional prognostic information and improve the pathological risk stratification system of GCs.

In the end of the study, we found that the predicted AHS stage was independently associated with disease-specific recurrence and long-term mortality. The prognosis was poor in those with higher-AHS stage even after radical resection. The AHS-based Cox model produced higher AUC than the eighth AJCC staging model for predicting disease-specific recurrence and mortality. Although the assessment of AHS might not make significant influence on patient management according to the current treatment guidelines for locally advanced GC because all these patients would undergo active surgery, from recent Japanese GC treatment guidelines, the endoscopic submucosal dissection, D1, or D1 gastrectomy is preferred in cT1 and cN0 cancers because of minimal injury, lower cost, high safety margin, and long-term excellent prognosis. In addition, neoadjuvant chemotherapy is recommended in those p-stage II or more categories before surgery. However, the major challenges exist on correctly defining the tumor stage on the base of the conventional imaging staging system. By this AHS staging scheme, "stage migration" might be reduced. Therefore, our study is an important preclinical step targeting for personalized medicine and prognostication.

Our study possesses several limitations. First, this was a retrospective and single center study. Further independent prospective multicenter validation cohort with large-scale data is needed to validate the robustness and ruggedness of our prediction model. Second, we did not include other possible risk factors, such as serological markers associated with GCs (33), and immunohistochemical features, such as Her-2, Ki67, and VEGFR-2 expression levels (34–36). If combined with other possible risk factors, the model may provide more accurate prognosis. Third, the median RFS and OS were relatively short, and we will improve this defect in our later work.

In conclusion, our study indicated that risk factors derived from our computational models could serve as strong biomarkers for preoperatively stratifying AHS in patients with GCs. Moreover, patients with high risk of histopathological status carried a worse prognosis. Therefore, our models incorporating radiographic and radiomic features might contribute to clinical decision support and personalized medicine in GCs.

CONFLICTS OF INTEREST

Guarantor of the article: Yu-Dong Zhang, MD, PhD and Xi-Sheng Liu, MD.

Specific author contributions: Conception and design: Y.D.Z and X.S.L. Development of methodology: Q.L., Q.X.F., C.L., L.Q., S.W.S., Y.S., G.Y., Y.D.Z., and X.S.L. Acquisition of data (acquired and managed patients, provided facilities, etc.): Q.L., Q.X.F., C.L., L.Q., S.W.S., Y.D.Z., and X.S.L. Analysis and interpretation of data (e.g., statistical analysis, biostatistics, and computational analysis): Q.L., L.Q., Q.X.F., C.L., S.W.S., J.Z., G.Y., Y.Q.G., Y.D.Z., and X.S.L. Writing, review, and/or revision of the manuscript: Q.L. and Y.D.Z. Administrative, technical, or material support (i.e., reporting or organizing data and constructing databases): Q.L., L.Q., Q.X.F., C.L., S.W.S., J.Z., G.Y., Y.Q.G., Y.D.Z., and X.S.L.

Financial support: This study is supported by China Postdoctoral Fund (2015M580453, Y.D.Z.) and a Key Social Development Program for the Ministry of Science and Technology of Jiangsu Province (BE2017756, Y.D.Z.).

Potential competing interests: None to report.

Study Highlights

WHAT IS KNOWN

- ✓ Because of no ideal histopathological risk-stratification method, the prognosis of patients with GCs with the same treatment regimen is still different.
- ✓ Generally, the histopathological status served as a prognostic indicator was assessed according to the patient's postoperative specimens.

WHAT IS NEW

- ✓ The computational model developed in this study combined large-scale radiographic and radiomic features, which can effectively predict whole histopathological status of GCs preoperatively.
- ✓ The model also further predicted the survival outcome successfully, achieving better performance than the eighth AJCC stage system.
- ✓ The computational model can be used as a prudent, valid, and accurate assessment tool for histopathological risk stratification in GCs noninvasively, which can accelerate the development of personalized, precision medicine.

TRANSLATIONAL IMPACT

- ✓ For patients with high AHS score, active adjuvant therapy might be recommended before surgery, and over treatment might be effectively avoided for patients with low AHS score.

REFERENCES

1. Fitzmaurice C, Fitzmaurice C, Dicker D, et al. The global burden of cancer 2013. JAMA Oncol 2015;1:505–27.
2. Torre LA, Bray F, Siegel RL, et al. Global cancer statistics 2012. CA Cancer J Clin 2015;65:87–108.
3. Van Cutsem E, Sagaert X, Topal B, et al. Gastric cancer. Lancet 2016;388: 2654–64.
4. Sano T, Coit DG, Kim HH, et al. Proposal of a new stage grouping of gastric cancer for TNM classification: International Gastric Cancer Association staging project. Gastric Cancer 2017;20:217–25.
5. Mihmanli M, Ilhan E, Idiz UO, et al. Recent developments and innovations in gastric cancer. World J Gastroenterol 2016;22: 4307–20.
6. Zhao LY, Chen XL, Wang YG, et al. A new predictive model combined of tumor size, lymph nodes count and lymphovascular invasion for survival prognosis in patients with lymph node-negative gastric cancer. Oncotarget 2016;7:72300–10.
7. Lazar D, Taban S, Sporea I, et al. Gastric cancer: Correlation between clinicopathological factors and survival of patients. II. Rom J Morphol Embryol 2009;50:185–94.
8. Hsu JT, Wang CW, Le PH, et al. Clinicopathological characteristics and outcomes in stage I-III mucinous gastric adenocarcinoma: A retrospective study at a single medical center. World J Surg Oncol 2016;14:123.
9. Zhu Z, Sun X, Wang J, et al. Histopathology-based prognostic score is independent prognostic factor of gastric carcinoma. BMC Cancer 2014;14: 663.
10. Taghavi S, Jayarajan SN, Davey A, et al. Prognostic significance of signet ring gastric cancer. J Clin Oncol 2012;30:3493–8.
11. Adachi Y, Yasuda K, Inomata M, et al. Pathology and prognosis of gastric carcinoma: Well versus poorly differentiated type. Cancer 2000;89: 1418–24.
12. Qiu MZ, Cai MY, Zhang DS, et al. Clinicopathological characteristics and prognostic analysis of Lauren classification in gastric adenocarcinoma in China. J Transl Med 2013;11:58.
13. Luo Y, Gao P, Song Y, et al. Clinicopathologic characteristics and prognosis of Borrmann type IV gastric cancer: A meta-analysis. World J Surg Oncol 2016;14:49.

14. An JY, Kang TH, Choi MG, et al. Borrmann type IV: An independent prognostic factor for survival in gastric cancer. J Gastrointest Surg 2008; 12:1364–9.
15. Du CY, Chen JG, Zhou Y, et al. Impact of lymphatic and/or blood vessel invasion in stage II gastric cancer. World J Gastroenterol 2012;18:3610–6.
16. Ma Z, Liang C, Huang Y, et al. Can lymphovascular invasion be predicted by preoperative multiphasic dynamic CT in patients with advanced gastric cancer? Eur Radiol 2017;27:3383–91.
17. Lee IS, Park YS, Lee JH, et al. Pathologic discordance of differentiation between endoscopic biopsy and postoperative specimen in mucosal gastric adenocarcinomas. Ann Surg Oncol 2013;20:4231–7.
18. Seevaratnam R, Cardoso R, McGregor C, et al. How useful is preoperative imaging for tumor, node, metastasis (TNM) staging of gastric cancer? A meta-analysis. Gastric Cancer 2012;15(Suppl 1):S3–18.
19. Fairweather M, Jajoo K, Sainani N, et al. Accuracy of EUS and CT imaging in preoperative gastric cancer staging. J Surg Oncol 2015;111:1016–20.
20. Li R, Li J, Wang X, et al. Detection of gastric cancer and its histological type based on iodine concentration in spectral CT. Cancer Imaging 2018;18:42.
21. Liu S, Liu S, Ji C, et al. Application of CT texture analysis in predicting histopathological characteristics of gastric cancers. Eur Radiol 2017;27:4951–9.
22. Ji GW, Zhang YD, Zhang H, et al. Biliary tract cancer at CT: A radiomics-based model to predict lymph node metastasis and survival outcomes. Radiology 2019;290:90–8.
23. van Griethuysen JJM, Fedorov A, Parmar C, et al. Computational radiomics system to decode the radiographic phenotype. Cancer Res 2017;77:e104–7.
24. Park H, Lim Y, Ko ES, et al. Radiomics signature on magnetic resonance imaging: Association with disease-free survival in patients with invasive breast cancer. Clin Cancer Res 2018;24:4705–14.
25. Japanese Gastric Cancer Association. Japanese gastric cancer treatment guidelines 2010 (ver. 3). Gastric Cancer 2011;14:113–23.
26. Amin MB, Greene FL, Edge SB, et al. The Eighth Edition AJCC Cancer Staging Manual: Continuing to build a bridge from a population-based to a more "personalized" approach to cancer staging. CA Cancer J Clin 2017; 67:93–9.
27. Huang CM, Xu M, Wang JB, et al. Is tumor size a predictor of preoperative N staging in T2-T4a stage advanced gastric cancer? Surg Oncol 2014;23:5–10.
28. Makino T, Fujiwara Y, Takiguchi S, et al. Preoperative T staging of gastric cancer by multi-detector row computed tomography. Surgery 2011;149:672–9.
29. Liu S, Shi H, Ji C, et al. Preoperative CT texture analysis of gastric cancer: Correlations with postoperative TNM staging. Clin Radiol 2018;73:756–e9.
30. Kim JI, Kim YH, Lee KH, et al. Type-specific diagnosis and evaluation of longitudinal tumor extent of Borrmann type IV gastric cancer: CT versus gastroscopy. Korean J Radiol 2013;14:597–606.
31. Li P, He HQ, Zhu CM, et al. The prognostic significance of lymphovascular invasion in patients with resectable gastric cancer: A large retrospective study from Southern China. BMC Cancer 2015;15:370.
32. Japanese Gastric Cancer Association. Japanese gastric cancer treatment guidelines 2014 (ver. 4). Gastric Cancer 2017;20:1–19.
33. Mihmanli M, Dilege E, Demir U, et al. The use of tumor markers as predictors of prognosis in gastric cancer. Hepatogastroenterology 2004; 51:1544–7.
34. Son HS, Shin YM, Park KK, et al. Correlation between HER2 overexpression and clinicopathological characteristics in gastric cancer patients who have undergone curative resection. J Gastric Cancer 2014;14: 180–6.
35. Seo SH, Kim KH, Oh SH, et al. Ki-67 labeling index as a prognostic marker in advanced stomach cancer. Ann Surg Treat Res 2019;96:27–33.
36. Peng J, Zhang J, Zhang Q, et al. A radiomics nomogram for preoperative prediction of microvascular invasion risk in hepatitis B virus-related hepatocellular carcinoma. Diagn Interv Radiol 2018;24:121–7.